Soft Matter

PAPER

View Article Online
View Journal | View Issue

Cite this: *Soft Matter*, 2026, **22**, 1340

Received 22nd September 2025, Accepted 8th January 2026

DOI: 10.1039/d5sm00959f

rsc.li/soft-matter-journal

Differing growth dynamics in seed-grown planar vertical chemical gardens

Mingchuan Zheng,[ab] Emmanuelle Dumont,[a] Romero D. Featherstone,[a] Nicholas Mackay,[ab] Herbert E. Huppert,[c] Julyan H. E. Cartwright*[de] and Alexander F. Routh*[ab]

Chemical gardens are self-assembled structures of semi-permeable precipitates. They are considered laboratory analogues of hydrothermal vents and can potentially be used for functional chemobrionic materials. In this work, the behaviour of chemical gardens grown from magnesium chloride seeds in sodium silicate solutions in a vertical Hele-Shaw cell has been investigated. The chemical gardens exhibited non-isotropic radial growth - fastest at the bottom and slowest at the top. In each direction, the radial growth can be modelled by a diffusion-controlled law. The relative pressure at the centre of the chemical garden underwent an initial, gradual growth, followed by a rapid increase that turned into a plateau. Upward tubular growth was observed for higher silicate concentrations, and the onset of upward tubular growth has been found to correlate with the onset of rapid pressurisation. The results may have implications on the formation mechanisms of hydrothermal vent flanges.

1. Introduction

Chemical gardens are self-assembled structures of semi-permeable precipitates formed by a set of reactive, non-equilibrium processes.[1–4] They were initially studied by Glauber in the 17th century, who dissolved a seed crystal of iron chloride in an aqueous solution of potassium silicate.[5] The name, "chemical gardens", arose from their plant-like appearance and growth mechanism, and the study of chemical gardens or their related phenomena is known as "chemobrionics".[1]

Interest in chemical gardens increased in the 1970s, when chemobrionic mechanisms were found in cement hydration processes.[6,7] Approximately at the same time, deep-sea hydrothermal vents were discovered on voyages by the naval submersible Alvin.[8,9] These submarine volcanic fissures came to be hypothesised as the sites for the origin of life on Earth and possibly elsewhere.[10–16] As chemical gardens and hydrothermal vents are physically and chemically similar, chemical gardens have been used as laboratory analogues of hydrothermal vents; conversely, hydrothermal vents have been viewed as natural chemical gardens.[17,18]

A key process in the formation of chemical gardens is the osmosis of water through the semi-permeable precipitates.[19,20] To give an example, when a crystal seed of metal chloride salt is placed at the bottom of a beaker containing an aqueous sodium silicate solution, the salt begins to dissolve, and the seed becomes covered by a layer of semi-permeable precipitate. This layer acts as a membrane, which is more permeable to water molecules and less permeable to the metal cations and the silicate anions. The osmotic pressure at the core is higher than the outside, causing water to flow inward from the outside silicate solution, which pressurises the membrane and ruptures it. As a result, a tubular, segmented, plant-like structure is created. This process is similar to the corrosion of metals.[21–23]

In order to investigate the dynamics of chemical garden formation and develop understanding of the growth of hydrothermal vents, a variety of experiments have been performed. Traditionally, chemical gardens are grown in three dimensions by placing a metal salt seed into an anion-containing solution.[24–32] The structures formed this way are often highly complex and difficult to analyse. For this reason, it is desirable to simplify the structures formed, and a way to achieve this is to reduce the dimensions in which chemical gardens are grown. Examples of this include microfluidic chips for quasi-1D growth,[33–38] as well as Hele-Shaw cells for quasi-2D growth.[39–52]

Hele-Shaw cells are devices made of two parallel plates separated by a small gap.[53] The small gap size renders the physics in the normal direction of the plates insignificant and

---

[a] *Department of Chemical Engineering and Biotechnology, University of Cambridge, Cambridge CB3 0AS, UK. E-mail: afr10@cam.ac.uk*
[b] *Institute for Energy and Environmental Flows, University of Cambridge, Cambridge CB3 0EZ, UK*
[c] *Department of Applied Mathematics and Theoretical Physics, University of Cambridge, Cambridge CB3 0WA, UK*
[d] *Instituto Andaluz de Ciencias de la Tierra, Consejo Superior de Investigaciones Científicas, E-18100 Granada, Spain. E-mail: julyan.cartwright@csic.es*
[e] *Instituto Carlos I de Física Teórica y Computacional, Universidad de Granada, E-18071 Granada, Spain*

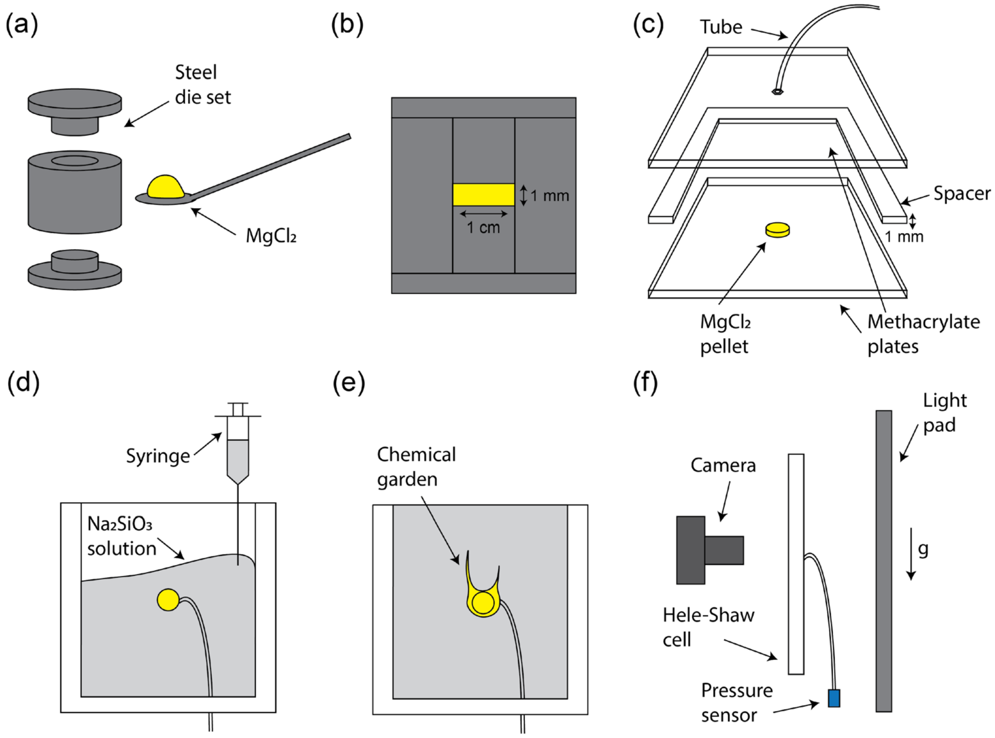

Fig. 1 Schematic of the experimental procedure. (a) and (b) 0.1850 g of $MgCl_2$ crystals are pressed into a cylindrical pellet with a 1.0 cm diameter and a 1.0 mm thickness. (c) The pellet is then placed at the centre of a Hele-Shaw cell made from two transparent plates separated by a 1.0 mm thick spacer. A thin plastic tube connects the centre of one plate to a relative pressure sensor. (d) and (e) The Hele-Shaw cell is then positioned vertically, with the opening at the top. A syringe is used to inject sodium silicate solution of a desired concentration into the cell until it is almost filled. (f) The cell is illuminated by a light pad and photographed by a camera.

the system quasi-two-dimensional.[54] Hele-Shaw cells are therefore versatile tools for studying problems involving viscous flows with chemical reaction.[55–60]

The present work focuses on chemical gardens grown from seeds in a vertical Hele-Shaw cell. Zheng *et al.*[52] showed that the growth of chemical gardens in a horizontal Hele-Shaw cell can be described by a diffusion-controlled model, before fracture due to osmotic pressurisation. This model assumes an isotropic circular geometry for the chemical garden pattern. Ding *et al.*[44] showed that, due to gravity, the chemical gardens in a vertical Hele-Shaw cell exhibit a systematic asymmetry between the upward direction – characterised by tubular growth – and the downward direction – characterised by bulk, finger-like growth. The present work aims to quantify these two growth regimes – in particular, to explore if the diffusional model found in the horizontal system is also applicable in the vertical system. A further goal is to confirm whether pressurisation and fracture are also present in the vertical system.

2. Experimental methods

The experiments were conducted using solid pellets made from magnesium chloride hexahydrate ($MgCl_2{\cdot}6H_2O$, ACS reagent, Sigma-Aldrich). A concentrated solution of sodium metasilicate (Na_2SiO_3, reagent grade, 1.39 g mL^{-1} at 25 °C, 26.5% SiO_2, Sigma-Aldrich) was diluted with deionised water into solutions of concentrations 0.2 M, 0.6 M, 1.0 M, 1.2 M, 1.4 M, 1.6 M, 1.8 M, and 2.2 M. For each silicate concentration, the experiment was repeated three times.

A schematic of the experimental procedure is shown in Fig. 1. First, 0.1850 g of $MgCl_2$ crystals are pressed into a cylindrical pellet with a 1.0 cm diameter and a 1.0 mm thickness using a steel die and a KBr Port-A-Press Kit (International Crystal Laboratories) under a pressure of 110 MPa for a minimum of 5 minutes. The pellet is then placed at the centre of a Hele-Shaw cell made from two methacrylate plates of dimensions 130 mm × 100 mm × 6 mm that are separated by a 1.0 mm thick spacer. A thin plastic tube connects the centre of one plate to a PS-2114 PASPORT Relative Pressure Sensor (PASCO Scientific) configured to measure the gauge pressure at the centre of the cell at a rate of 20 Hz. The Hele-Shaw cell is then positioned vertically, with an opening at the top end. A syringe is used to inject sodium silicate solution of a desired concentration into the cell until it is almost filled. The cell is illuminated by a light pad and photographed every 20 seconds by a Nikon D5300 digital single-lens reflex (DSLR) camera with a resolution of 6000 pixels × 4000 pixels. The chemical garden is allowed to grow for a minimum of two hours. All experiments were carried out in a laboratory maintained at 20 °C.

3. Representative experiment

Fig. 2 shows results for a representative experiment performed with a $MgCl_2$ pellet in a 1.2 M Na_2SiO_3 solution. Photographs of

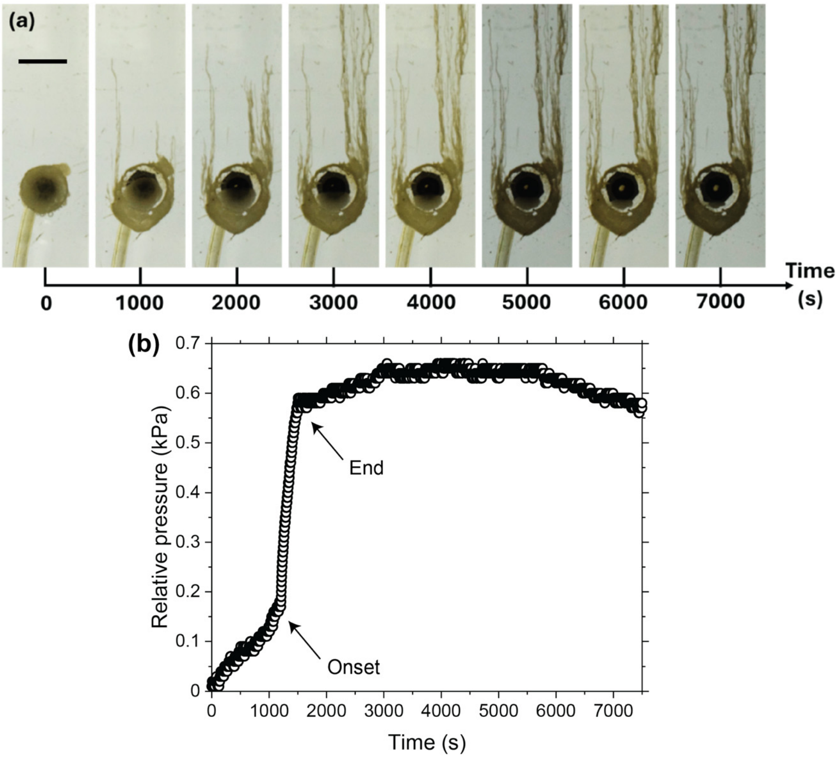

Fig. 2 Results for a representative experiment performed with a $MgCl_2$ pellet in a 1.2 M Na_2SiO_3 solution. (a) Photographs of the experiment taken every 1000 s, where gravity was operating downwards. The scale bar is 1 cm long. (b) Plot of the relative pressure at the centre throughout the experiment. A sharp increase can be observed at approximately 1200 s whose points of onset and end are marked by arrows.

the experiment taken every 1000 s are shown in Fig. 2a, and a video is available in the supplementary information (SI). In these photographs, gravity was operating downwards. After the pellet was submerged in the silicate solution, it began to dissolve. The resulting solution then reacted with the silicate solution to produce a precipitate. From the images, it can be seen that the growth was non-uniform. Initially, bulk growth occurred in all directions: fastest in the downward direction, followed by the horizontal left and right directions, and the slowest in the upward direction. After some time, thin ''tubes'' or ''filaments'' started to preferentially grow upward from the side of the upper precipitate layer. These structures resemble classical chemical gardens,[19] albeit with an additional downward growth, as they are not constrained below.

Fig. 2b displays a plot of the relative pressure measured at the centre of the Hele-Shaw cell throughout the experiment. The pressure gradually increased until approximately 1200 s, at which point there was a sudden sharp increase from approximately 0.18 kPa to 0.58 kPa. The points of onset and end of this sharp increase are marked on the figure. The elevated pressure was maintained until the end of the experiment at 7500 s. This is expected and due to the osmotic flow of water from the outer silicate solution into the centre of the chemical garden. A similar sharp increase in pressure was also observed in the horizontal Hele-Shaw experiments by Ding *et al.*[39] and Zheng *et al.*[52]. Ding *et al.*[39] argued that this is a case of a chemical clock reaction. There, the pressurisation coincided with the fracture of the chemical garden, exhibiting a spike that gradually decreased back. Here, however, no visible fracture was observed in the chemical garden in Fig. 2a; instead of exhibiting a spike, the pressure after the rapid increase did not decrease back and reached a plateau as seen in Fig. 2b.

4. Final chemical garden structures

The results obtained from the experiment in 1.2 M Na_2SiO_3 solution were also generally obtained in experiments with other silicate concentrations. The pressure evolved with time in three regimes - a slow, linear, initial increase, followed by a rapid increase, followed by a plateau. Fig. 3a shows the images obtained from experiments in silicate solutions of various concentrations at 3000 s. This time was selected as it was generally in the region of pressure plateau, and any further observed growth was not significant. The growth patterns can be separated into two regimes: 0.2 M to 1.0 M, and 1.2 M to 1.8 M. In the first regime, the silicate solution was relatively dilute, and the growth was predominantly downward, with little to no tubular growth in the upward direction. In particular, at 0.2 M, the precipitate grew all the way downwards, reaching the bottom of the Hele-Shaw cell and forming a structure that was vastly different from all others. In the latter regime, the solution was more concentrated, and significant amount of tubular growth was observed which occurred preferentially from the side of the upper precipitate layer.

The density of a saturated aqueous solution of $MgCl_2$ at room temperature and atmospheric pressure is approximately

1.25 g mL^{-1},[61] whereas the densities of the Na_2SiO_3 solutions used in this work are in the range of 1.03 g mL^{-1} to 1.15 g mL^{-1}.[44] At the centre of the chemical garden, the shrinking pellet continuously supplies $MgCl_2$, making the solution at the centre and in the close vicinity of the pellet to be effectively a saturated solution of $MgCl_2$. Therefore, we believe that at lower silicate concentrations, the inner, denser $MgCl_2$ solution moved downward due to gravity. When the silicate concentration was higher, the density difference between the inner and outer solutions was smaller. Osmotic pressurisation of the chemical garden centre, which fractured parts of the top thin layer, could drive $MgCl_2$ solution upward through the small cracks, forming tubular structures. The $MgCl_2$ solution responsible for the upward tubular growth was likely unsaturated and less dense than the outer silicate solution.

In many previous studies of seed-grown chemical gardens, the seed was placed at the bottom of a vessel—for example, a crystal salt placed in a beaker containing sodium silicate solution – where the majority of growth occurred upward as tubular structures.[62–64] But when the seed is suspended in the middle of the vessel, as in this study, downward growth can be significant.

5. Pressure results

Fig. 3b and c show the results of the time and relative pressure at the onset and end of the region of rapid pressurisation, corresponding to the points marked on Fig. 2b for the experiment in 1.2 M silicate solution. Fig. 3b presents the average times of pressurisation against the concentration of silicate, and Fig. 3c presents the average values of relative pressure during pressurisation against the concentration of silicate. In both figures, the data do not exhibit an obvious trend against silicate concentration. There is also no significant difference between the behaviours at the onset and end of pressurisation. Nonetheless, two regimes can be observed separated at 1.0 M silicate concentration which roughly correspond to the two distinct growth regimes observed in Fig. 3b. For experiments conducted with silicate concentrations below 1.0 M, it seemed that the results were more reproducible as seen by the smaller error bars; in this regime, the time at which pressurisation occurred appeared to increase with silicate concentration.

6. Image analysis

To quantify the observed chemical garden growth, we analysed the photographs with the Image Processing Toolbox™ on MATLAB (MathWorks). Two types of analysis were performed on the images: radial growth and upward tubular growth. The radial growth analysis was carried out by examining the thickness of the precipitate layer in four orthogonal directions – up, down, left, and right. The upward tubular growth was assessed by calculating the area covered by the precipitate tubes above the bulk of the chemical garden.

6.1. Radial growth

An example of the image analysis procedure for the radial growth is shown in Fig. 4 for an experiment performed in 1.0 M silicate solution. The program first identifies the circular pellet to determine its radius, r_0 = 0.5 cm, and the coordinates

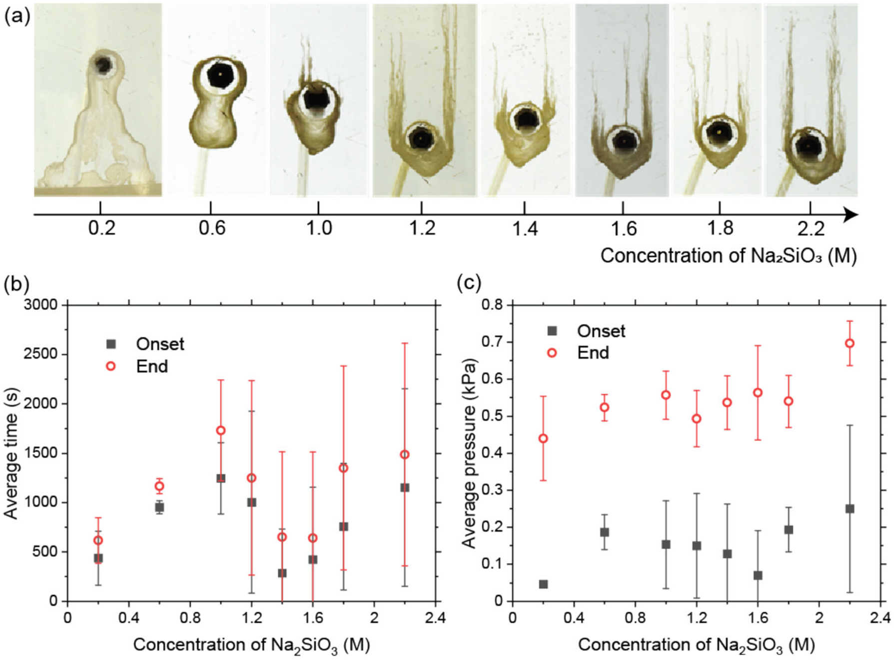

Fig. 3 (a) Photographs of experiments in silicate solutions of various concentrations at 3000 s. (b) Plots of the average times at the onset and end of pressurisation against silicate concentration. (c) Plots of the average values of the relative pressure at the onset and end of pressurisation against silicate concentration. The error bars are the sample standard deviations.

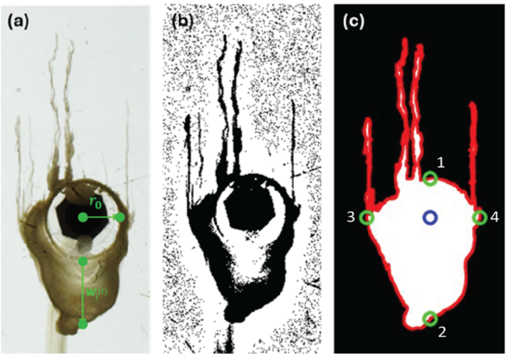

Fig. 4 An example of the radial growth image analysis procedure for an experiment performed in 1.0 M silicate solution. (a) The program identifies the circular pellet to determine its radius, r_0 = 0.5 cm, and the coordinates of its centre (green dot at the centre). (b) Once cropped, the image is then binarised. (c) The pixels corresponding to the precipitate pattern's edge are identified (red curve). The coordinates of the circle centre (blue dot) are set as the origin to obtain the locations of the edge of the precipitate in both the horizontal and vertical directions (green circles), given as $r_i(t)$, where $i \in [1, 2, 3, 4]$ represents the up, down, left, and right directions, respectively. The radius r_0 is subtracted from $r_i(t)$ to calculate the thickness of the pellet in that direction, $w_i(t)$. This process is repeated for all images.

of its centre (indicated by the green dot at the centre on Fig. 4a and the blue circle on Fig. 4c). This is an important step for obtaining a suitable crop of the picture, because the pressure sensor tube is similar in colour to the precipitate and could interfere with the analysis. Once cropped, the image is binarised, and the output is shown in Fig. 4b. The pixels corresponding to the precipitate pattern's edge are identified (represented by the red curve in Fig. 4c), and the coordinates of the circle centre are set as the origin to obtain the locations of the edge of the precipitate in both the horizontal and vertical directions (represented by the green circles in Fig. 4c), given as $r_i(t)$, where $i \in [1, 2, 3, 4]$ represents the up, down, left, and right directions, respectively. The radius r_0 is subtracted from $r_i(t)$ to calculate the thickness of the precipitate layer in that direction, $w_i(t)$. This process is repeated for all images.

A plot of $w_i(t)$ in all four directions for this experiment conducted in 1.0 M silicate solution is shown in Fig. 5a. It can be seen that, while the chemical garden grew in all directions, it did not do so isotropically and varied across the four directions. The upward radial growth was the smallest, and the downwards radial was the largest, which aligns with expectation due to the influence of gravity: in the range of silicate concentrations studied, saturated $MgCl_2$ is denser than the outer silicate solution. The growths in the left and right directions were intermediate. Furthermore, growth in the horizontal directions was largely, albeit not completely, symmetrical. Growth in all directions ceased after certain time – about 3000 s in the bottom and left directions and 2000 s in the top and right – after which the value of $w_i(t)$ reached a plateau.

Previously, Zheng *et al.*[52] concluded that the radial growth of a horizontal chemical garden is well described by a diffusional growth law, whereby the diffusion of metal cations from the shrinking seed pellet controlled the rate of precipitate growth

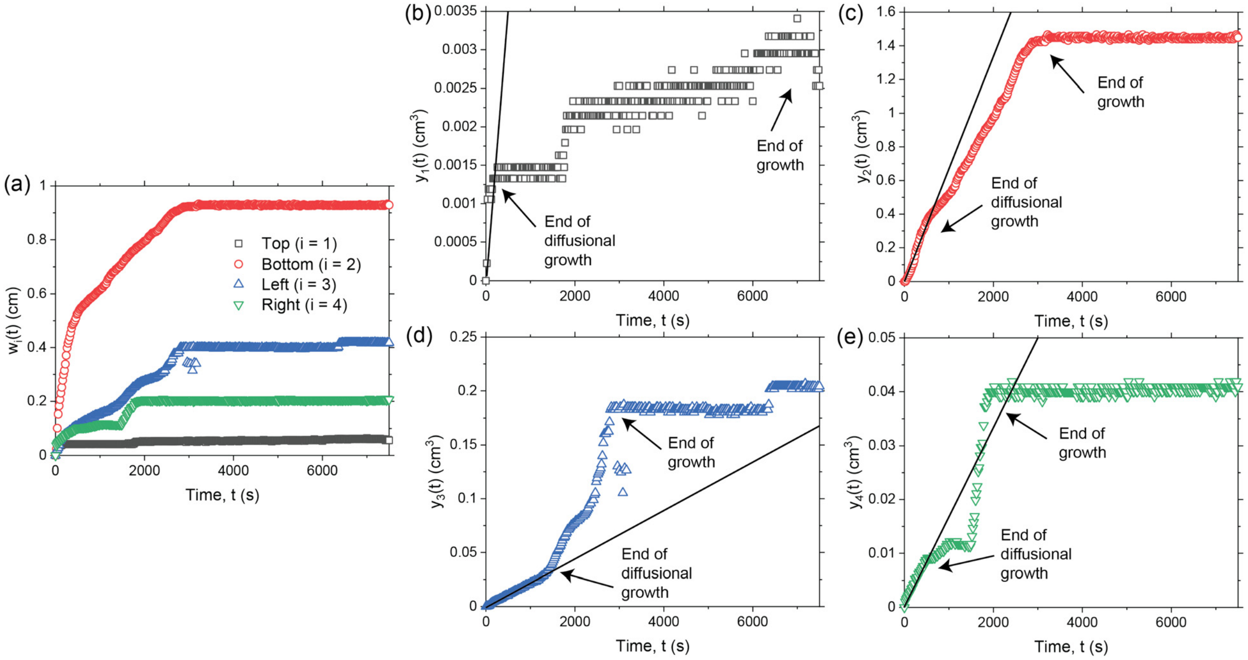

Fig. 5 (a) A plot of $w_i(t)$ in all four directions for an experiment conducted in 1.0 M silicate solution, where $i \in [1, 2, 3, 4]$ represents the up, down, left, and right directions, respectively. $w_i(t)$ grew with varying rates across the four directions. Growth in all directions ceased at a certain point - about 3000 s in the bottom and left directions and 2000 s in the top and right - after which the value of $w_i(t)$ reached a plateau. (b)–(e) Plots of $y_i(t) = w_i^3(t) + 3r_0w_i^2(t)/2$ for the same experiment. Initial growth of $y_i(t)$ against time was linear in all the four directions, where the solid lines represent the linear fits, suggesting that the early growth of $w_i(t)$ can be described by the diffusion-controlled law described in the work of Zheng *et al.*[52] The approximate points when the diffusion-controlled regime ended and when the radial growth itself ended are marked by arrows.

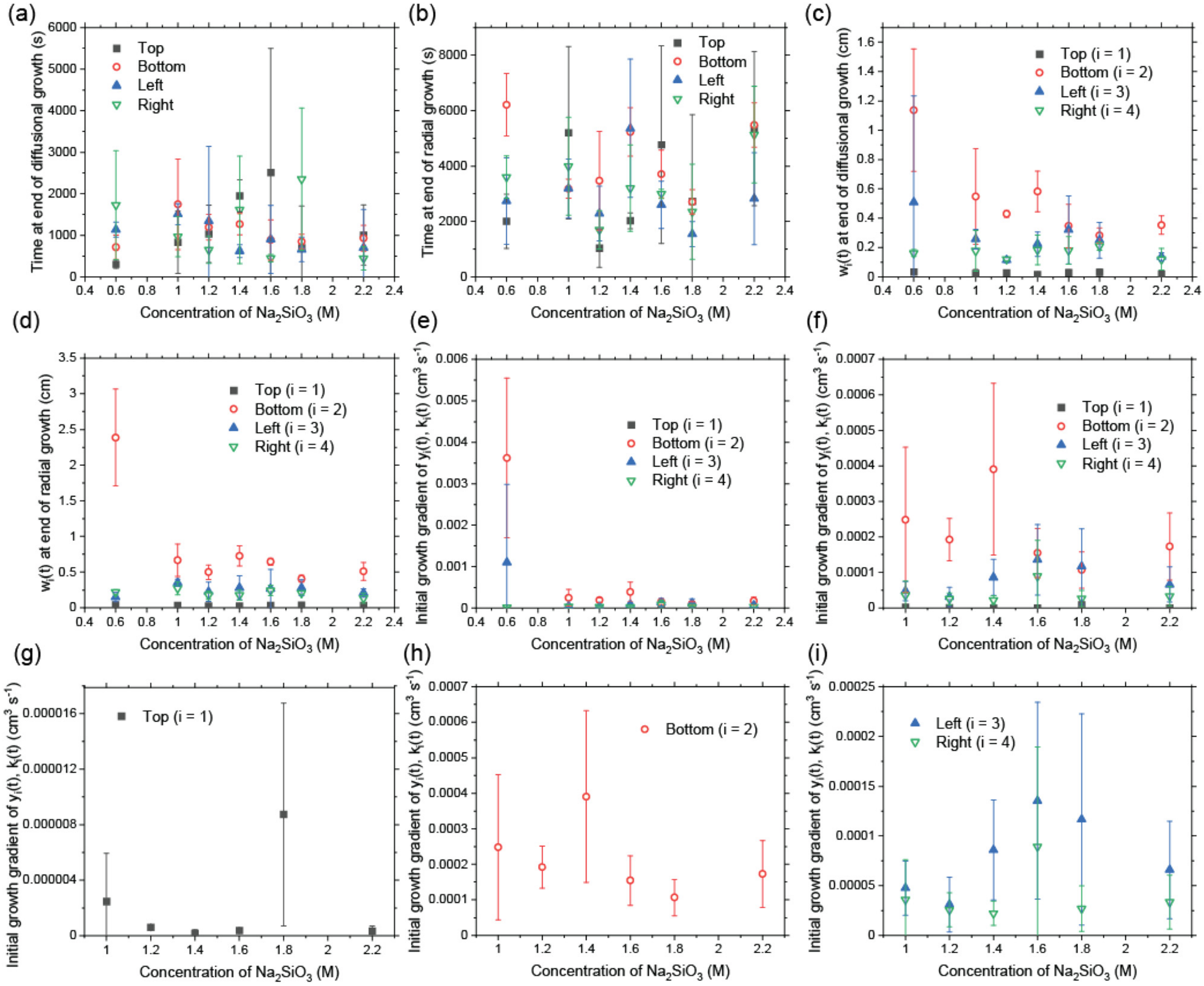

Fig. 6 The average results of $w_i(t)$ and $y_i(t)$ for all experiments apart from those carried out in 0.2 M silicate solutions which exhibited very fast downward growths. (a) Plots of the average times at the end of the diffusion-controlled regime against silicate concentration. (b) Plots of the average times at which radial growth stopped entirely against silicate concentration. (c) Plots of the average values of $w_i(t)$ at the end of the diffusion-controlled regime in the four radial directions against silicate concentration. (d) Plots of the average values of $w_i(t)$ at the end of radial growth in the four radial directions against silicate concentration. (e) Plots of the average gradients of $y_i(t)$, k_i, at the end of the diffusion-controlled regime for the four radial directions. (f)–(i) The same results as (e) but without data obtained from 0.6 M experiments. The error bars are the sample standard deviations.

until the precipitate layer fractured due to osmosis. Assuming that $w_i(t)$ in the vertical geometry of this study also follows the same law, then

$$y_i(t) = w_i^3(t) + \frac{3}{2} r_0 w_i^2(t) = k_i t. \quad (1)$$

Here, $w_i^3(t) + 3r_0 w_i^2(t)/2$ is grouped into a single function $y_i(t)$ in the direction i. If this model holds, $y_i(t)$ should be proportional to time, with k_i as the proportionality constant. Fig. 5b–d show how $y_i(t)$ evolves with time for the experiment conducted in 1.0 M in the four directions. In these figures, at early time, the growth of $y_i(t)$ was linear in all the four directions (the solid lines represent the linear fits). The results suggest that the diffusion-type growth model can be applied to the vertical geometry for the initial growth of the chemical gardens. The approximate points when the diffusion-controlled regime ended and when the radial growth itself ended are marked on the graphs. Similar behaviours of $w_i(t)$ and $y_i(t)$ are found in data obtained from experiments conducted with different silicate concentrations.

Fig. 6 shows plots for the average results of $w_i(t)$ and $y_i(t)$ for all experiments apart from those carried out in the 0.2 M silicate solutions which exhibited very fast downward growth. Fig. 6a shows plots of the average times at the end of the diffusion-controlled regime against the concentration of the silicate employed. Fig. 6b shows the average times at which radial growth stopped entirely against silicate concentration. In both Fig. 6a and b, no clear trend can be deduced.

Fig. 6c presents the average values of the precipitate thickness, $w_i(t)$, at the end of the diffusion-controlled regime in the four radial directions against silicate concentration. Fig. 6d presents the average values of $w_i(t)$ at the end of the radial growth. It is evident that the precipitate layer at the bottom was the thickest across all concentrations, and the thickness at the top was the thinnest. Additionally, the bottom thickness decreased with increasing silicate concentration. The likely reason is, when the silicate solution is more concentrated, it becomes more dense, and the density difference between the inner and outer solutions becomes smaller, which limits downward growth. The values of $w_i(t)$ on the left and right directions are similar to each other for most concentrations, except for 0.6 M. Since growth in the horizontal directions are not affected by gravity, it is not surprising that the two directions are largely symmetric to each other. Overall, no visible trend is discerned for the values of $w_i(t)$ with varying silicate concentration.

Fig. 6e displays plots of the average gradients of $y_i(t)$, k_i, at the end of the diffusion-controlled regime for the four radial directions. Due to large error bars for the 0.6 M silicate solutions, the same plots without 0.6 M are presented in Fig. 6f and individually in Fig. 6g–i. k_i indicates the growth rate of $w_i(t)$ in direction i. The results show that growth was fastest in the bottom layer, intermediate in the left and right horizontal layers, and slowest in the top layer. Growth rates in the bottom and horizontal directions are orders of magnitude faster than in the top direction. For the bottom layer, the gradient of $y_2(t)$, k_2, decreases as the silicate concentration increases. However, no observable pattern can be concluded in the growth behaviours in the other directions.

6.2. Tubular growth

The image analysis procedure for the tubular growth of an example experiment performed in a 1.6 M silicate solution is illustrated in Fig. 7. As for the radial growth, the location and radius of the circular pellet is first identified, shown by the red circle. The picture is cropped just slightly above where the pellet is located, as shown by the green rectangle in Fig. 7a. The image is then binarised, as shown on Fig. 7b. The number of pixels corresponding to the precipitate in the cropped area is counted, as illustrated in Fig. 7c, and this value is converted into cm^2. This process is repeated for all the experiments performed with silicate concentrations above 1.0 M, where tubular growths were observed. Fig. 7d shows the results obtained from the experiment performed with 1.6 M silicate solution. The graph reveals an initial time offset before growth started, followed by a linear increase in tubular area. Results from the first 1000 s show the details of the initial time offset of 400 s in Fig. 7e. The plateau observed at around 2500 s corresponds to the tubes reaching the top of the experimental set-up and is not related to the plateaus seen in the relative pressure and radial growth graphs.

Plots of the average times at which the tubular growth began against silicate concentration is shown in Fig. 7f. The average times at the onset and end of pressurisation for this silicate

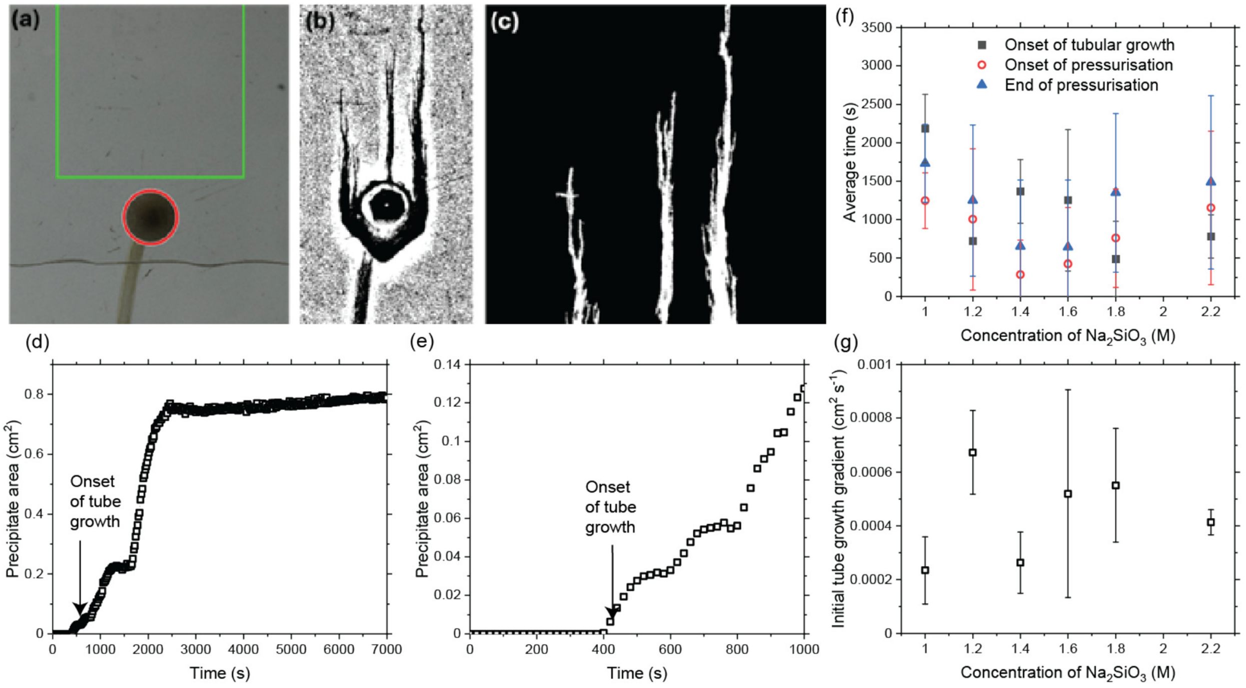

Fig. 7 Schematic of the image analysis procedure for the tubular growth of an example experiment performed in a 1.6 M silicate solution at 4000 s. (a) The location and radius of the circular pellet is identified (red circle). The picture is suitably cropped above where the pellet is located (green rectangle). (b) The image is binarised. (c) The number of pixels corresponding to the precipitate in the cropped area is counted. (d) The number of pixel obtained is converted into cm^2 and plotted against time. An initial time offset of 400 s before growth was observed, followed by a linear increase in tubular growth. The plateau observed at around 2500 s corresponds to the tubes reaching the top of the experimental set-up and is not related to the plateaus seen in relative pressure and radial growths graphs. (e) The same results as (d) but only for the first 1000 s to show the details of the initial time offset of 400 s. (f) Plots of the average times at which the tubular growth began against silicate concentration. The average times at the onset and end of pressurisation against silicate concentration are reproduced from Fig. 3b and also shown here. (g) Plots of the average growth gradients of the tubes at the onset of growth across different silicate concentrations. The error bars are the sample standard deviations.

concentration range are also shown on the same figure, reproduced from Fig. 3b. It can be seen that there is likely a relationship between the time at which tubular growth occurs and the time at which pressurisation begins, suggesting that the growth of the tubes is driven by the pressure at the centre of the chemical garden. As the inner, saturated $MgCl_2$ solution has a higher chemical potential than the outside silicate solution, water on the outside flows inward through the semi-permeable precipitate, giving rise to a pressure buildup. Since the top layer is the thinnest, as seen in Fig. 6, small cracks open up on the top layer after a given time. Through these small cracks, some unsaturated $MgCl_2$ solution can be ejected, which forms tubular structures upon reaction with silicate. This is in contrast to the horizontal experiments, where the pressurisation catastrophically fractures the precipitates layer at a random location.

Fig. 7g displays the average growth gradients of the tubes at the onset of growth across different silicate concentrations. No clear pattern emerges.

7. Conclusions

Chemical gardens have been grown in a vertical Hele-Shaw cell from solid magnesium chloride pellets in solutions of sodium silicate. All chemical gardens exhibit non-isotropic radial growths, with the growth on the bottom the fastest and on the top the slowest. In each direction, the radial growth initially follows a diffusion-controlled model similar to horizontal experiments. In all experiments, the relative pressure sensed at the centre underwent an initial, gradual growth, followed by a rapid increase which turned into a plateau. No fracture was observed, in contrast to what was observed in the horizontal configuration. For experiments with silicate concentrations greater than 1.0 M, upward tubular growths were observed, and the time at which tubular growth initiates is correlated with the time of rapid pressurisation.

Further investigations can focus on developing mechanical laws for the temporal evolution of the relative pressure at the centre of the Hele-Shaw cell and the growth dynamics of the tubes. In addition, the concentration profile of the seed salt in the interior solution can be studied *via* techniques such as UV-vis spectroscopy. The large lateral tubular growths observed in this work are visually similar to hydrothermal vent flanges,[65,66] and this may mean that seed-grown chemical gardens in vertical Hele-Shaw cells can act as good laboratory analogues for studying the behaviour of hydrothermal vent flanges.

Author contributions

M. Z.: conceptualisation, formal analysis, investigation, methodology, software, supervision, writing – original draft, writing – review and editing; E. D.: formal analysis, investigation, software, writing – original draft, writing – review and editing; R. F.: formal analysis, investigation, software, writing – original draft, writing – review and editing; N. M.: software, formal analysis; H. E. H.: formal analysis, supervision, writing – review and editing; J. H. E. C.: conceptualisation, formal analysis, funding acquisition, methodology, supervision, writing – review and editing; A. F. R.: conceptualisation, formal analysis, funding acquisition, methodology, supervision, writing – review and editing.

Conflicts of interest

There are no conflicts to declare.

Data availability

The raw photographs and relative pressure measurements obtained from the experiments are deposited on Apollo, the University of Cambridge Repository. See DOI: https://doi.org/10.17863/CAM.125152. All other data are included in the article and/or supplementary information (SI). Supplementary information: video of a representative experiment performed with a $MgCl_2$ pellet in a 1.2 M Na_2SiO_3 solution. See DOI: https://doi.org/10.1039/d5sm00959f.

Acknowledgements

The authors acknowledge the financial support from the European Cooperation in Science and Technology Action CA21169 Dynalife.

References

1 L. M. Barge, S. S. S. Cardoso, J. H. E. Cartwright, G. J. T. Cooper, L. Cronin, A. De Wit, I. J. Doloboff, B. Escribano, R. E. Goldstein, F. Haudin, D. E. H. Jones, A. L. Mackay, J. Maselko, J. J. Pagano, J. Pantaleone, M. J. Russell, C. I. Sainz-Díaz, O. Steinbock, D. A. Stone, Y. Tanimoto and N. L. Thomas, *Chem. Rev.*, 2015, **115**, 8652–8703.
2 S. S. S. Cardoso, J. H. E. Cartwright, J. Čejková, L. Cronin, A. De Wit, S. Giannerini, D. Horváth, A. Rodrigues, M. J. Russell, C. I. Sainz-Díaz and A. Tóth, *Artif. Life*, 2020, **26**, 315–326.
3 J. Čejková and J. H. E. Cartwright, *ChemSystemsChem*, 2022, **4**, e202200002.
4 C. Pimentel, M. Zheng, J. H. E. Cartwright and C. I. Sainz-Díaz, *ChemSystemsChem*, 2023, **5**, e202300002.
5 J. R. Glauber, *Furni Novi Philosophici,* Joannem Janssonium, Amsterdam, The Netherlands, 1658.
6 D. D. Double and A. Hellawell, *Nature*, 1976, **261**, 486–488.
7 R. D. Coatman, N. L. Thomas and D. D. Double, *J. Mater. Sci.*, 1980, **15**, 2017–2026.
8 P. Lonsdale, *Deep-Sea Res.*, 1977, **24**, 857–863.
9 J. B. Corliss, J. Dymond, L. I. Gordon, J. M. Edmond, R. P. von Herzen, R. D. Ballard, K. Green, D. Williams, A. Bainbridge, K. Crane and T. H. van Andel, *Science*, 1979, **203**, 1073–1083.

10 S. Holler, S. Bartlett, R. J. G. Löffler, F. Casiraghi, C. I. Sainz Diaz, J. H. E. Cartwright and M. M. Hanczyc, *Proc. Natl. Acad. Sci. U. S. A.*, 2023, **120**, e2300491120.

11 T. Matreux, P. Aikkila, B. Scheu, D. Braun and C. B. Mast, *Nature*, 2024, **628**, 110–116.

12 C. M. Gutiérrez-Ariza, L. M. Barge, Y. Ding, S. S. S. Cardoso, S. E. McGlynn, R. Nakamura, D. Giovanelli, R. Price, H. E. Lee, F. J. Huertas, C. I. Sainz-Díaz and J. H. E. Cartwright, *Prog. Earth Planet. Sci.*, 2024, **11**, 11.

13 H.-E. Lee, T. Okumura, H. Ooka, K. Adachi, T. Hikima, K. Hirata, Y. Kawano, H. Matsuura, M. Yamamoto, M. Yamamoto, A. Yamaguchi, J.-E. Lee, H. Takahashi, K. T. Nam, Y. Ohara, D. Hashizume, S. E. McGlynn and R. Nakamura, *Nat. Commun.*, 2024, **15**, 8193.

14 P. Rimmer and O. Shorttle, *J. Colloid Interface Sci.*, 2024, **14**, 498.

15 C. Liu, W. Xu, Z. Zhang, K. Robinson, M. Lau, F. Huang, F. Huang, C. R. Glein and J. Hao, *Astrophys. J.*, 2024, **971**, 51.

16 F. Westall, *Philos. Trans. R. Soc. B*, 2025, **380**, 20240106.

17 M. J. Russell, A. J. Hall and D. Turner, *Terra Nova*, 1989, **1**, 238–241.

18 T. C. Marlin, J. M. Weber, R. Y. Sheppard, S. Perl, D. Diener, M. M. Baum and L. M. Barge, *Chem*, 2025, **11**, 102289.

19 J. H. E. Cartwright, J. M. Garca-Ruiz, M. L. Novella and F. Otálora, *J. Colloid Interface Sci.*, 2002, **256**, 351–359.

20 C. Pimentel, C. Gutiérrez-Ariza, A. G. Checa, C. I. Sainz-Díaz and J. H. E. Cartwright, *Phys. Chem. Miner.*, 2024, **51**, 7.

21 F. Brau, F. Haudin, S. Thouvenel-Romans, A. De Wit, O. Steinbock, S. S. S. Cardoso and J. H. E. Cartwright, *Phys. Chem. Chem. Phys.*, 2018, **20**, 784–793.

22 L. M. Silva-Bedoya, E. Watkin and L. L. Machuca, *Mater. Corros.*, 2021, **72**, 1138–1151.

23 J. Jiang, N. Li, B. Wang, F. Liu, C. Liu and X. Cheng, *Metals*, 2024, **14**, 652.

24 C. Pimentel, J. H. E. Cartwright and C. I. Sainz-Díaz, *ChemSystemsChem*, 2020, **2**, e2000023.

25 B. Busupalli and V. K. Patel, *Chem. Commun.*, 2022, **58**, 4172–4175.

26 V. K. Patel and B. Busupalli, *Chem. Commun.*, 2023, **59**, 768–771.

27 V. Patel, M. Patel, B. Busupalli and A. Solanki, *Langmuir*, 2024, **40**, 2311–2319.

28 P. Farkas, E. Lantos, D. Horváth and A. Tóth, *ChemSystemsChem*, 2024, **6**, e202400053.

29 B. A. Guler, Z. G. Morçimen, S. Tas Demir, Z. Demirel, E. Turunç, A. S. Endemir and E. Imamoglu, *Sci. Rep.*, 2024, **14**, 13764.

30 M. C. Reis, *ACS Omega*, 2025, **10**, 9496–9502.

31 M. Podbielski, P. Knoll, G. Brown, S. Huld, A. Neubeck, J. H. E. Cartwright, C. I. Sainz-Díaz, C. Pimentel and S. McMahon, *Geobiology*, 2025, **23**, e70021.

32 S. Reigl, E. Wagner, C. Pimentel, W. Kunz, A. E. S. Van Driessche and M. Kellermeier, *Angew. Chem., Int. Ed.*, 2025, **64**, e202508098.

33 B. C. Batista and O. Steinbock, *J. Phys. Chem. C*, 2015, **119**, 27045–27052.

34 Y. Ding, B. Batista, O. Steinbock, J. H. E. Cartwright and S. S. S. Cardoso, *Proc. Natl. Acad. Sci. U. S. A.*, 2016, **113**, 9182–9186.

35 Q. Wang, M. R. Bentley and O. Steinbock, *J. Phys. Chem. C*, 2017, **121**, 14120–14127.

36 P. S. Eastham, M. N. J. Moore, N. G. Cogan, Q. Wang and O. Steinbock, *J. Fluid Mech.*, 2020, **888**, A20.

37 Q. Wang and O. Steinbock, *Langmuir*, 2021, **37**, 2485–2493.

38 D. Spanoudaki, F. Brau and A. De Wit, *J. Solid State Electrochem.*, 2025.

39 Y. Ding, C. M. Gutiérrez-Ariza, C. I. Sainz-Díaz, J. H. E. Cartwright and S. S. S. Cardoso, *Angew. Chem., Int. Ed.*, 2019, **58**, 6207–6213.

40 Y. Ding, J. H. E. Cartwright and S. S. S. Cardoso, *Phys. Rev. Fluids*, 2020, **5**, 082201.

41 L. A. M. Rocha, J. H. E. Cartwright and S. S. S. Cardoso, *Phys. Chem. Chem. Phys.*, 2021, **23**, 5222–5235.

42 L. A. M. Rocha, J. H. E. Cartwright and S. S. S. Cardoso, *Chaos*, 2022, **32**, 053107.

43 L. A. M. Rocha, L. Thorne, J. J. Wong, J. H. E. Cartwright and S. S. S. Cardoso, *Langmuir*, 2022, **38**, 6700–6710.

44 Y. Ding, C. M. Gutiérrez-Ariza, M. Zheng, A. Felgate, A. Lawes, C. I. Sainz-Díaz, J. H. E. Cartwright and S. S. S. Cardoso, *Phys. Chem. Chem. Phys.*, 2022, **24**, 17841–17851.

45 Y. Kubodera, Y. Xu, Y. Yamaguchi, M. Matsuo, M. Fujii, M. Kageyama, O. Steinbock and S. Nakata, *Phys. Chem. Chem. Phys.*, 2023, **25**, 12974–12978.

46 B. C. Batista, A. Z. Morris and O. Steinbock, *Proc. Natl. Acad. Sci. U. S. A.*, 2023, **120**, e2305172120.

47 S. Testón-Martínez, T. Huertas-Roldán, P. Knoll, L. M. Barge, C. I. Sainz-Díaz and J. H. E. Cartwright, *Phys. Chem. Chem. Phys.*, 2023, **25**, 30469–30476.

48 M. Weingart, S. Chen, C. Donat, V. Helmbrecht, W. D. Orsi, D. Braun and K. Alim, *Sci. Adv.*, 2023, **9**, eadi188.

49 S. Tanaka, K. Otoguro, M. Kunihiro, H. Ishikawa and Y. Sumino, *Phys. Rev. E*, 2024, **109**, 065105.

50 K. Otoguro, K. Yoshii and Y. Sumino, *Phys. Fluids*, 2024, **36**, 063105.

51 Y. Kubodera, M. Matsuo and S. Nakata, *Phys. Chem. Chem. Phys.*, 2025, **27**, 18454–18458.

52 M. Zheng, P. R. L. Welche, S. S. S. Cardoso, H. E. Huppert, J. H. E. Cartwright and A. F. Routh, *Philos. Trans. R. Soc., A*, 2025, **383**, 20240266.

53 H. Hele-Shaw, *Nature*, 1898, **58**, 34–36.

54 O. Logvinov, *Acta Astronaut.*, 2016, **123**, 103–108.

55 L. A. M. Rocha, C. Gutiérrez-Ariza, C. Pimentel, I. Sánchez-Almazo, C. I. Sainz-Díaz, S. S. S. Cardoso and J. H. E. Cartwright, *Geochem., Geophys., Geosyst.*, 2021, **22**, e2021GC009724.

56 H. E. Huppert and S. S. Pegler, *J. Fluid Mech.*, 2022, **932**, A5.

57 K. P. Deshmukh, D. Arlov, R. S. Cant, A. Göransson, F. Innings and D. I. Wilson, *Food Bioprod. Process.*, 2022, **136**, 84–96.

58 Y. Ding, J. H. E. Cartwright and S. S. S. Cardoso, *Geobiology*, 2024, **22**, e12611.

59 Y. Nagatsu and A. De Wit, *J. Fluid Mech.*, 2025, **1016**, R3.

60 K. P. Deshmukh, A. T. Bagdziunas, R. S. Cant, D. Arlov and D. I. Wilson, *Chem. Eng. Sci.*, 2026, **321**, 122829.

61 S. Al Ghafri, G. C. Maitland and J. P. M. Trusler, *J. Chem. Eng. Data*, 2012, **57**, 1288–1304.

62 J. H. E. Cartwright, B. Escribano and C. I. Sainz-Díaz, *Langmuir*, 2011, **27**, 3286–3293.

63 J. H. E. Cartwright, B. Escribano, C. I. Sainz-Díaz and L. S. Stodieck, *Langmuir*, 2011, **27**, 3294–3300.

64 P. Knoll, B. C. Batista, S. McMahon and O. Steinbock, *ACS Earth Space Chem.*, 2022, **6**, 2644–2650.

65 A. W. Woods and J. R. Delaney, *Earth Planet. Sci. Lett.*, 1992, **112**, 117–129.

66 S. K. Goffredi, S. Johnson, V. Tunnicliffe, D. Caress, D. Clague, E. Escobar, L. Lundsten, J. B. Paduan, G. Rouse, D. L. Salcedo, L. A. Soto, R. Spelz-Madero, R. Zierenberg and R. Vrijenhoek, *Proc. R. Soc. B*, 2017, **284**, 20170817.